*Sensors & Transducers, Vol. 273, Issue 2, June 2026, pp. 1-10*

www.sensorsportal.com

**Sensors & Transducers**

Published by IFSA Publishing, S. L., 2026
http://www.sensorsportal.com

# A Simulation Study of Novel Piezo-MOS and Current Mirror Integrated Microbridge Mass Sensor for Low Mass Sensing Applications

**[1, *] Menuvolu TETSEO, [1] Kalpana GOGOI, [1] Gaurav KUMAR, [2] Shashi KUMAR and [1] Pradeep Kumar RATHORE**

[1] Department of Electronics and Communication Engineering, National Institute of Technology Meghalaya, Sohra 793108, India

[2] Micron Technology Operation India LLP, Hyderabad, Telangana 500032, India

[*] E-mail: P21EC008@nitm.ac.in

*Received: 26 Jan. 2026 /Revised: 20 March 2026 /Accepted:27 May 2026 /Published: 29 June 2026*

**Abstract:** The article presents a MEMS microbridge integrated with two identical MOSFETs in a current mirror configuration. The input MOSFET, embedded on the substrate, serves as a reference MOSFET, while the output MOSFET is placed at the fixed edge of the microbridge to detect deflection-induced mechanical stress. Due to the piezoresistive effect, applied mass changes the channel mobility of the output MOSFET, resulting in changes in drain current and voltage across its drain terminals. Three microbridge-based sensing configurations are investigated: (a) pMOS channel resistive loaded, (b) nMOS channel resistive loaded and (c) dual channel current mirror integrated microbridge mass sensors. Simulation using COMSOL Multiphysics and TSpice software shows sensitivity of approx. 0.11 µV/µg, 2.33 µV/µg and 12.67 µV/µg for pMOS, nMOS and dual channel sensors, respectively. Fabrication process steps and mask-layout design are also discussed. Overall, this study demonstrates a promising and robust approach for highly sensitive low-mass sensing applications.

**Keywords:** Microelectromechanical systems, Piezoresistive devices, Current mirror circuit, Sensor systems.

## 1. Introduction

Over the years, a significant amount of research has been dedicated to Microelectromechanical System (MEMS) based biosensors [1-5]. A key area of focus within this research is the detection of small masses, particularly in the field of biomedical and chemical applications. Integrating sensors alongside a readout circuit on a single chip is highly preferable and instrumental in achieving high sensitivity and precision in detecting small masses. This integration can be facilitated by the CMOS-MEMS technology [6-13]. CMOS-MEMS enables seamless integration of the MEMS sensor with CMOS readout circuit, leading to improved performance, noise reduction, and various other benefits such as miniaturization, cost-effectiveness, reduced power consumption and rapid response times.

Mass sensors using MEMS structures such as diaphragm, microcantilever and microbridge have been reported by researchers worldwide [13-17]. The MEMS microbridge structure consists of a beam with two fixed edges and two free edges. When load is applied, the microbridge undergoes deflection and stress is induced at its fixed edges. This stress can be measured using different transduction solutions like piezoresistive [11], piezoelectric [18], capacitive [17], and optical transduction mechanism [19]. Each of these methods faces inherent limitations like temperature sensitivity, noise and nonlinearity when operated under adverse environmental conditions [20]. Recent years have seen the integration of FETs with

MEMS, where researchers have reported several studies exploiting the piezoresistive effect in MOSFETs [21–24]. This piezoresistive effect in silicon MOSFET arises due to distortion of energy band upon application of load. This distortion affects the effective mass, which in turn affects the electron and hole mobility, and hence its resistivity [25]. This piezo-MOS transduction mechanism is an inherent property of MOSFETs and remains relatively unexplored, leaving a significant scope for further investigation using CMOS circuit as sensor readout circuits.

In this context, one promising approach is the use of MOSFET-based current mirror as sensor readout circuit [24, 26–29]. While commonly used as biasing circuit, current mirrors have shown to offer several advantages when used as a readout circuit such as temperature compensation, seamless interfacing and full CMOS compatibility. This eliminates the need for complex ΔR/R measurements and additional temperature compensation circuit, unlike other works reported in the literature [30–32]. Prior studies have demonstrated the efficiency of this approach in pressure sensors [26–29], and most recent work demonstrated cantilever-based piezo-MOS sensing under tip loading [24]. In the present study, the same sensing concept is applied to a microbridge structure under central loading, introducing a different mechanical boundary condition. This changes the governing equations and stress distribution, with symmetric stress generated at both fixed edges, resulting in a distinct electromechanical response.

From the literature [33], microbridge structures offer advantages over microcantilevers due to their double-clamped configuration, including better mechanical stability, lower sensitivity to residual fabrication stress, easier sensing-layer deposition, and improved MEMS integration. They also exhibit higher resonant frequency and mass sensitivity. While microcantilevers are preferred for large deflection and very low mass sensing, microbridges are suitable for applications requiring higher stability and larger mass range. However, the present work is limited to a proof-of-concept study on integrating a microbridge structure with a MOSFET sensing element and a current mirror readout circuit for low-mass sensing applications, focusing only on the static behavior of the sensor under constant mass-loading conditions.

## 2. Design and Modelling

### 2.1. Physical Structure and Working Principle

The proposed mass sensor consists of a microbridge beam as its mechanical mass sensing element. This study introduces three different mass sensor configurations, shown in Fig. 1: (a) resistive loaded p-channel MOSFET based current mirror integrated mass sensor, (b) resistive loaded n-channel MOSFET based current mirror integrated mass sensor, (c) dual channel MOSFET current mirror integrated mass sensor. In the p-channel and n-channel sensors, two identical MOSFETs are arranged in a resistive loaded current mirror configuration. These sensors consist of one reference MOSFET (Mp1/Mn1) positioned on the substrate and one stress sensing MOSFET (Mp2/Mn2) placed on one fixed edge of the bridge. Resistors are connected to the drain terminals of both the reference and output MOSFET branches to provide resistive loading. The dual channel mass sensor consists of four MOSFETs, with Mp1 and Mn1 serving as reference MOSFETs, while Mp2 and Mn2 act as stress sensing MOSFETs. The current mirror circuits were designed using the 5 µm CMOS technology parameters given in Table 1. These parameters were selected to analyze the proposed circuit under long-channel operating conditions, where current mirror behavior and stress-induced mobility variation can be examined without additional complexity from advanced device scaling effects.

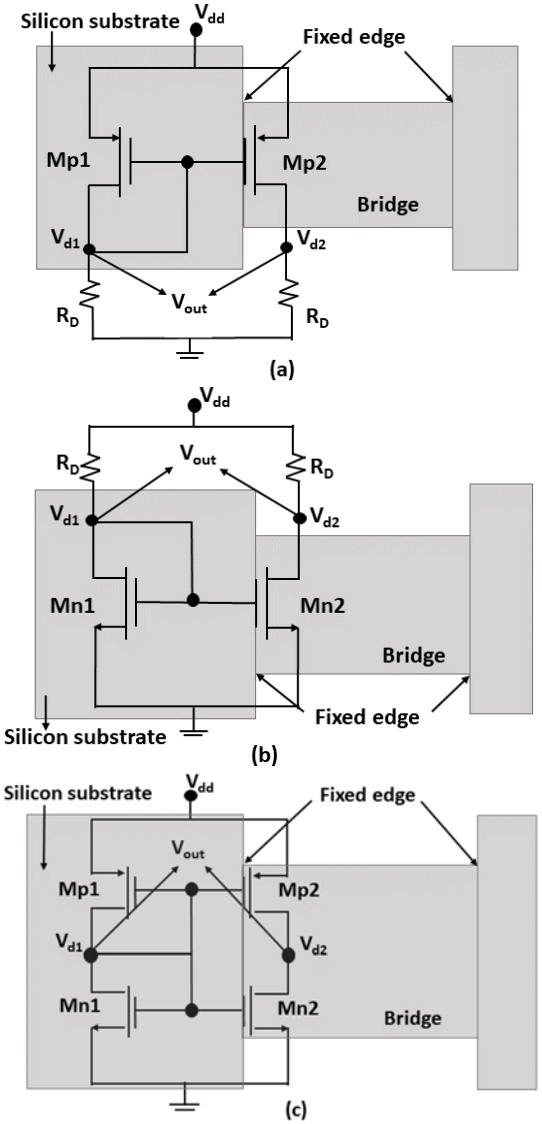


**Fig. 1.** (a) pMOS channel resistive loaded; (b) nMOS channel resistive loaded, and (c) dual channel current mirror integrated microbridge mass sensors.

**Table 1.** Parameters of 5 μm CMOS technology [34].

| Parameters | p-MOSFET | n-MOSFET |
|---|---|---|
| Mobility ($cm^2$/Vs) | 250 | 750 |
| Threshold voltage (V) | -1 | 1 |
| Thickness of gate oxide (nm) | 85 | 85 |
| Supply voltage (V) | 10 | 10 |
| Oxide capacitance (fF/μ$m^2$/Vs) | 0.406 | 0.406 |
| Early voltage (V/ μm) | 6.67 | 20 |
| Transconductance (μA/$V^2$) | 10.15 | 30.45 |

The cross-sectioned view of the proposed bridge sensor under no-load and applied load condition is illustrated in Fig. 2. Upon applying mass load, the bridge undergoes deflection, inducing stress at its fixed edges. This leads to a change in mobility of the output MOSFET (Mp2/Mn2), and consequently its drain voltage and current, while the mobility of the reference MOSFET (Mp1/Mn1) remains the same and unaffected by load. The output voltage corresponding to external load can be calculated between the drain terminals of the reference MOSFET M1 and output MOSFET M2. In all three sensor configurations, the reference MOSFET is diode-connected, establishing the gate bias for the corresponding sensing transistor.

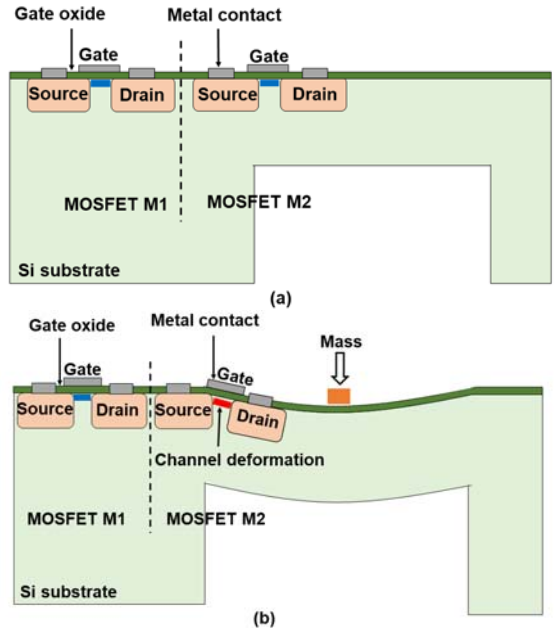


**Fig. 2.** The cross-sectional view of the microbridge sensor under: (a) no load condition and (b) applied load condition.

## 2.2. Theoretical Model

### a) Micromechanical Element: Microbridge

The proposed sensor incorporates a silicon microbridge with its dimension parameters given in Table 2. The maximum displacement ($W_{max}$) and stress ($T_{max}$) for the bridge under load conditions are given in equations 1 and 2 [35].

$$W_{\max} = \frac{Mg}{Ebh^3} x^2 \left(\frac{3}{2} a_1 - x\right), \tag{1}$$

$$T_{\max} = \frac{3a_1}{2bh^2} Mg, \tag{2}$$

where $b$ and $h$ are breadth and height of bridge, $E$ is the Young's modulus, $M$ represents central mass of the bridge, $x$ is the original position of the beam and $a_1$ is the distance of the central mass from the fixed ends of the bridge.

**Table 2.** Parameters used to design and simulate the proposed current mirror bridge based mass sensors.

| Parameters | p-MOSFET | n-MOSFET |
|---|---|---|
| MOSFET Channel length and width | Length = 10 μm<br>Width = 20 μm | |
| Microbridge dimension (Length, breadth, height) | (200, 100, 5) μm | |
| Drain resistor ($R_D$) | 11.94 kΩ | 17.73 kΩ |
| Resistance of MOSFET piezoresistor | 197.92 kΩ | 593.46 kΩ |
| Piezoresistive coefficient ($10^{-12}$ $Pa^{-1}$) | $\pi_{11}$ = -66<br>$\pi_{12}$ = 11<br>$\pi_{44}$ = -1380 | $\pi_{11}$ = 1020<br>$\pi_{12}$ = -534<br>$\pi_{44}$ = 136 |
| Mass load | In range of 0 to 100 μg, with step size of 10 μg | |

### b) Transduction Mechanism

The proposed sensor uses the piezoresistive effect in MOSFET as the transduction mechanism. As reported in a previous work [26], the pMOS and nMOS are designed as a simple piezoresistor where its resistance is equal to MOSFET's channel resistance ($R_{ch} = r_o = V_A/I_D$). [25] reported that under externally applied load, the mobility changes alone create a drain current change of the MOSFET. Hence, the carrier mobility and corresponding drain currents of both the pMOS and nMOS under load condition are given as

$$\frac{\Delta\mu_p}{\mu_p} = \frac{\Delta\mu_n}{\mu_n} = \frac{\Delta R_{ch}}{R_{ch}} = -\pi\sigma, \tag{3}$$

$$I_{Dp} = (\mu_p \pm \Delta\mu_p) C_{ox} \frac{W}{L} \frac{(V_{SG} - V_{tp})^2}{2}, \tag{4}$$

$$I_{Dn} = (\mu_n \pm \Delta\mu_n) C_{ox} \frac{W}{L} \frac{(V_{GS} - V_{tn})^2}{2}, \tag{5}$$

where $\mu$ denotes the carrier mobility, $\Delta\mu$ is the change in carrier mobility under applied load, $\pi$ is the piezoresistive coefficient, while $\sigma$ is the stress

developed in the MOSFET channel region. $L$ and $W$ denote channel length and width respectively, $C_{ox}$ is the oxide capacitance per unit area. $V_{GS}$ is the gate-to-source voltage, while $V_{tp}$ and $V_{tn}$ represent the threshold voltages of the p- and n-channel MOSFETs, respectively.

**c) Readout Circuit**

The output voltage corresponding to external load can be calculated between the drain terminals of the reference MOSFET M1 and the output MOSFET M2

$$V = V_{DS1} - V_{DS2} = -\pi\sigma I_{D1} R_D, \quad (6)$$

where $V_{DS1}$ and $V_{DS2}$ represent drain-to-source voltages of MOSFET M1 and M2, respectively.

All the MOSFETs were biased to operate in the saturation region. The mathematical model of the readout circuit has been described and explained in [24, 26].

## 3. Simulation Results

COMSOL Multiphysics was employed to simulate the mass sensing bridge structure while the analysis of the electrical behavior of the current mirror circuit was done using TSpice simulation tool. The parameters employed for simulations are given in Table 2. The simulation starts with the construction of a 3D mass sensing bridge structure integrated with strain sensing MOSFET equivalent piezoresistors. Subsequently, the material properties, mechanical and electrical boundary conditions, and meshing of the sensor structure were defined. Input voltages corresponding to the threshold voltages of the pMOS and nMOS transistors were applied across their respective equivalent piezoresistors. Mass load was then applied to the bridge structure, and simulations were conducted to analyze the piezoMOS behavior of the proposed mass sensors. Fig. 3 and Fig. 4 illustrate the maximum displacement and stress profiles of the microbridge structure obtained from COMSOL Multiphysics. Under a load of 100 µg, the microbridge structure undergoes a maximum deflection of 0.207 nm at the center and maximum stress of 65.3 kPa at the fixed edges.

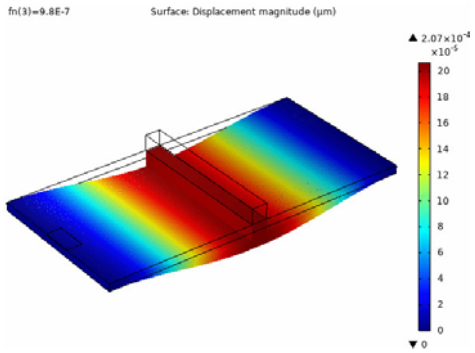


**Fig. 3.** Displacement profile of a microbridge structure under 100 µg load.

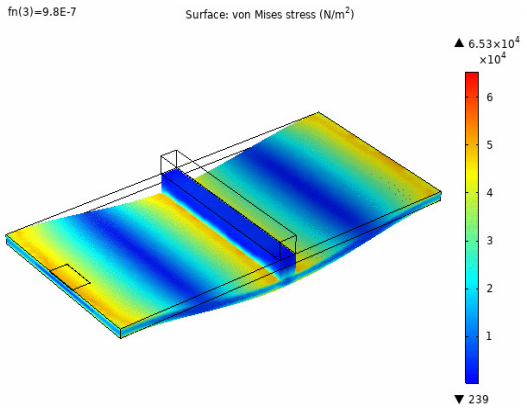


**Fig. 4.** Stress profile of a microbridge structure under 100 µg load.

The variations in channel resistance and mobility were obtained. These mobility values were subsequently used in TSpice simulation tool to determine the drain currents and voltages of the current mirror readout circuit. In order to study the effect of thickness of MOSFET equivalent piezoresistor, simulation was performed for five piezoMOS thicknesses for both pMOS and nMOS. Under an input load of 100 µg, pMOS and nMOS equivalent piezoresistors gives a change of (0.00088, 0.00086, 0.00079, 0.00079, 0.00072) $cm^2/Vs$ and (0.0331, 0.0320, 0.0309, 0.0285, 0.0267) $cm^2/Vs$ in its channel mobilities for piezoMOS thickness of (0.1, 0.25, 0.5, 0.75, 1) µm, respectively. Fig. 5 and Fig. 6 show the variations in channel mobility and resistance of pMOS and nMOS equivalent piezoresistors, respectively, with different values of piezoMOS thickness. The results showed that mobility and resistance changes are higher with smaller piezoMOS thickness. However, simulation of structures with one dimension significantly smaller than the others may result in meshing and convergence issues [36]. Therefore, piezoMOS thickness of 0.5 µm was selected for this study [26].

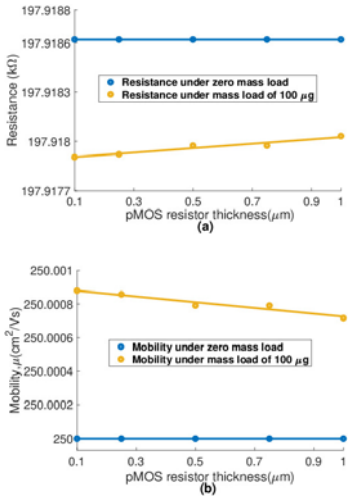


**Fig. 5.** Plot of: (a) channel resistance and (b) channel mobility with respect to resistor thickness of pMOS.

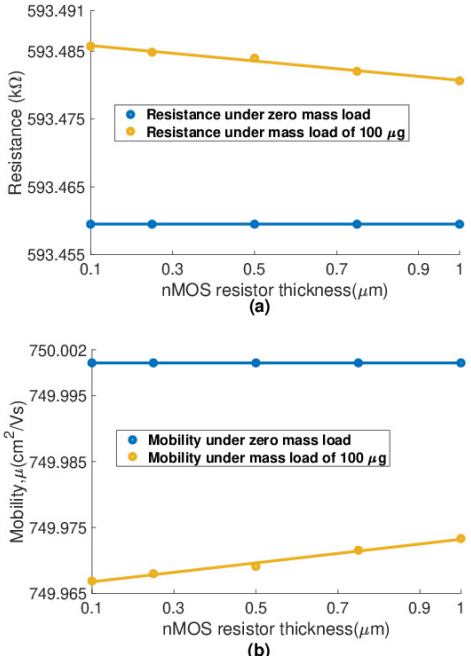


**Fig. 6.** Plot of: (a) channel resistance and (b) channel mobility with respect to resistor thickness of nMOS.

A mesh convergence analysis using nine mesh sizes was conducted to evaluate simulation accuracy, with results summarized in Table 3. The output voltage plot with respect to the number of meshing elements is given in Fig. 7. The graph shows that the voltage output starts to saturate after 'coarse' mesh size, meaning any mesh size ranging from 'coarse' to 'extremely fine' produced convergent result. Hence, we have conducted this study with 'finer' mesh size, which lies within the range of converged result, affirming its accuracy.

**Table 3.** Results from meshing analysis.

| Meshing size | No. of meshing elements | Output voltage (μV) | % variation in output voltages |
|---|---|---|---|
| Extremely coarse | 444 | 150 | - |
| Extra coarse | 944 | 220 | 46.667 |
| Coarser | 1630 | 220 | 0 |
| Coarse | 3135 | 230 | 4.545 |
| Normal | 6370 | 230 | 0 |
| Fine | 13704 | 230 | 0 |
| Finer | 19863 | 230 | 0 |
| Extra fine | 32511 | 230 | 0 |
| Extremely fine | 77173 | 230 | 0 |

When mass is loaded on the bridge beam, it results in a change of channel resistance and channel mobility of all three mass sensors. The piezoMOS effect, described by [25], was used to study channel resistance and mobility change. Fig. 8 (a-c) show the channel resistance change for the pMOS, nMOS and dual channel mass sensors with varying load, respectively. Under a 100 μg load, the pMOS sensor showed a reduction of approx. 0.6 Ω, nMOS sensor showed an increase of approx. 24.5 Ω, while dual mass sensor showed a decrease of approx. 0.6 Ω and enhancement of approx. 24.6 Ω for its pMOS and nMOS equivalent resistor, respectively.

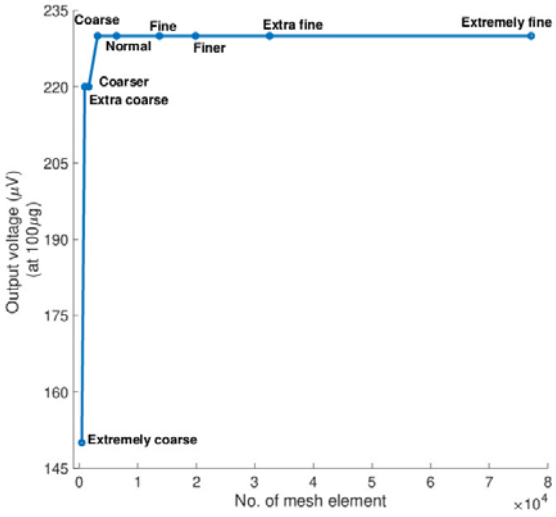


**Fig. 7.** Graph of output voltage with respect to number of mesh elements.

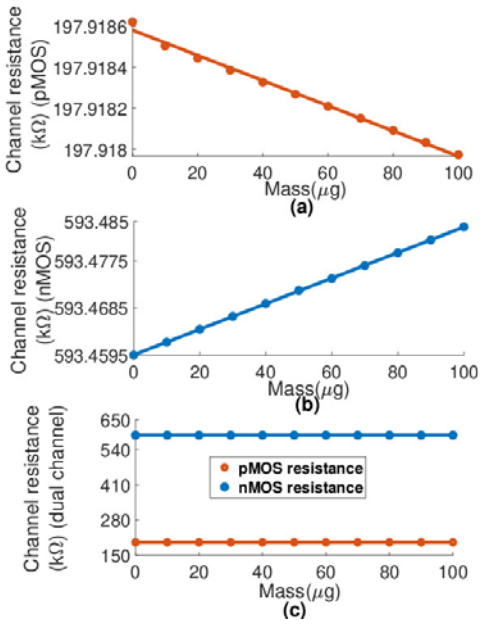


**Fig. 8.** Graph of channel resistance vs mass for: (a) pMOS, (b) nMOS and (c) dual channel mass sensor.

Fig. 9 (a-c) show the change in the channel mobility for the pMOS, nMOS and dual channel mass sensors, respectively. Under 100 μg load, the pMOS experiences an increase of approx. 0.0008 $cm^2/Vs$ while the nMOS undergoes a decrease of approx. 0.0309 $cm^2/Vs$. The dual sensor showed an increase of

approx. 0.0008 $cm^2/Vs$ and a decrease of approx. 0.0311 $cm^2/Vs$ for the pMOS and nMOS, respectively. This channel mobility obtained from COMSOL Multiphysics was then used in TSpice simulation tool to calculate the electrical properties of the mass sensors. The reference MOSFETs remains independent of load applied, while output MOSFETs acts as a function of external load. Therefore, drain currents and voltages of the output MOSFETs will change under load, while those of reference MOSFETs remain the same. Under 100 µg load, the pMOS experience an increase of 0.001 µA in its drain current while the nMOS and dual channel mass sensors show a reduction of approximately 0.01 µA in its drain current. This variation in the drain current is shown in Fig. 10 (a-c).

Fig. 11 (a-c) illustrate the drain voltage change of the three sensors under varying mass load. An increase in the drain voltage of approx. 0.00005 V, 0.00023 V and 0.00127 V was noted for the pMOS, nMOS and dual channel mass sensors, respectively. The plots of differential output voltage proportional to the input mass load for pMOS, nMOS, and dual channel mass sensors are depicted in Fig. 12 (a-c). The pMOS, nMOS and dual channel mass sensors give a sensitivity of 0.11 µV/µg, 2.33 µV/µg, and 12.67 µV/µg, respectively.

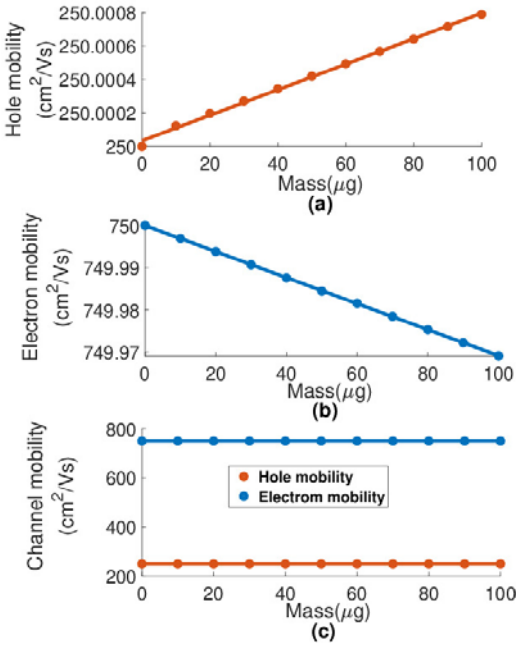


**Fig. 9.** Graph of channel mobility vs mass for: (a) pMOS, (b) nMOS and (c) dual channel mass sensor.

The higher sensitivity of dual channel sensor over the other two sensors can be attributed to the fact that the dual sensor incorporates two sensing elements, while pMOS and nMOS mass sensor have only one sensing element. In addition, the higher sensitivity of nMOS over pMOS mass sensor is due to the piezoresistive effect. It has been reported that devices with n-type show better piezo resistivity in both longitudinal and transverse direction as compared to p-type device [37]. Table 4 summarizes the electrical parameters of both the reference and output MOSFET for each sensor configuration under a 100 µg load.

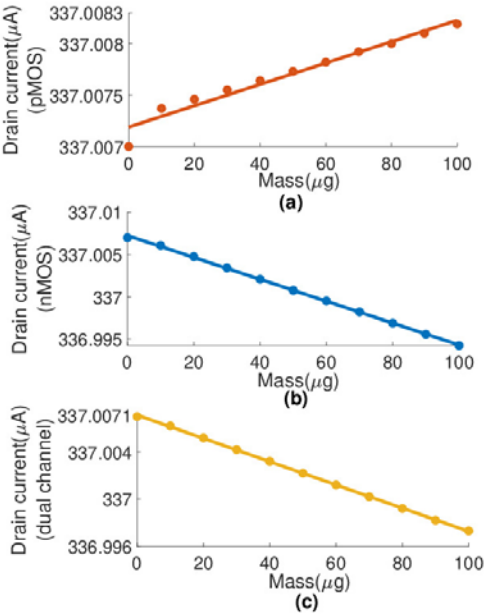


**Fig. 10.** Graph of drain current vs mass for: (a) pMOS, (b) nMOS and (c) dual channel mass sensor.

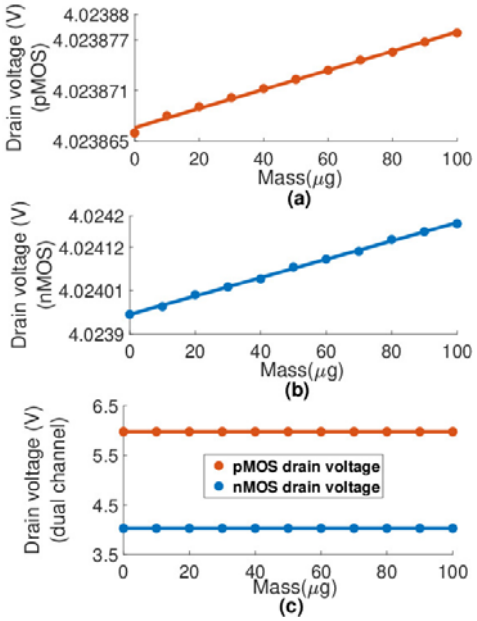


**Fig. 11.** Graph of drain voltage with respect to mass for: (a) pMOS, (b) nMOS and (c) dual channel mass sensor.

Additional performance metrics including noise, limit of detection (LOD), resolution, and linearity were calculated for all three sensor configurations. Noise was evaluated using the Johnson–Nyquist

relation [38] based on the equivalent MOSFET channel resistance. At 300 K for 1 Hz bandwidth, the calculated RMS noise voltages are 57.3 nV for the pMOS sensor, 99.3 nV for the nMOS sensor, and 114.6 nV for the dual-channel sensor. The corresponding LOD values are 1.56 µg, 0.128 µg, and 0.027 µg, respectively. The estimated resolutions are 0.52 µg, 0.043 µg, and 0.009 µg for the pMOS, nMOS, and dual-channel sensors, respectively. Linearity is assessed by linear regression of output voltage versus applied mass, yielding $R^2$ values of 0.9959, 0.9987, and 0.9999 for the pMOS, nMOS, and dual-channel sensors, respectively. These results demonstrate excellent linearity across the entire sensing range.

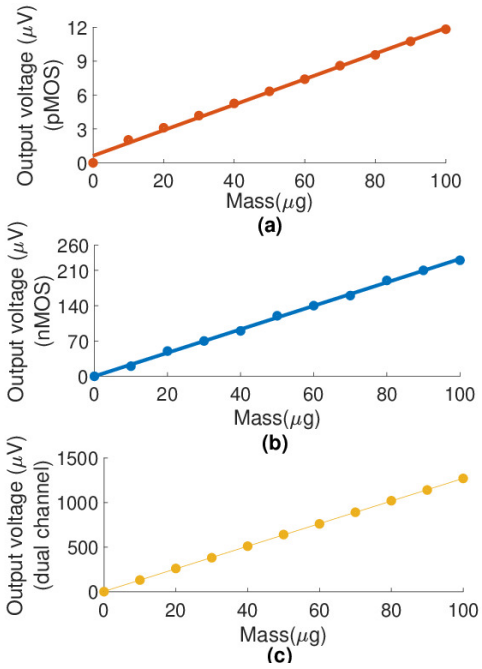


**Fig. 12.** Graph of output voltage with respect to mass for: (a) pMOS, (b) nMOS and (c) dual channel mass sensor.

To further evaluate temperature stability, the sensors are simulated at temperatures of 300 K, 325 K, and 350 K. Table 5 summarizes the corresponding electrical characteristics for all three sensor configurations under a load of 100 µg. The results show that channel resistance, mobility, and drain voltages vary with temperature across all three sensors. However, the calculated sensitivities remain stable over the investigated temperature range. This occurs because both the reference and sensing MOSFETs undergo similar temperature-dependent variations in their device parameters. Consequently, the current mirror output largely cancels these common shifts, providing inherent temperature compensation within the simulated range.

The proposed fabrication process flow of the pMOS mass sensor is shown in Fig. 13. The process starts with dry oxidation on an RCA-cleaned silicon wafer to grow the field oxide (Fig. 13 (a)). The first lithography step patterns the source-drain regions (Fig. 13 (b)), followed by source-drain doping (Fig. 13 (c)). Subsequently, another lithography process defines the gate oxide region (Fig. 13 (d)), followed by the growth of gate oxide (Fig. 13 (e)). A third lithography process patterns the contact vias (Fig. 13 (f)), while the fourth lithography process forms the metal lines and contact pads (Fig. 13 (g)), followed by metallization and the lift-off process (Fig. 13 (h)). The front side of the wafer is then coated with photoresist to protect the circuit (Fig. 13 (i)). The backside window is then patterned by the fifth lithography step, followed by DRIE etching of backside silicon (Fig. 13 (j)). Subsequently, the front side of the bridge structure is defined using a sixth lithography step, followed by DRIE etching of silicon to release the structure (Fig. 13 (k)). Finally, removal of photoresist from both top and bottom layers (Fig. 13 (l)) completes the fabrication of the sensor. The fabrication process flow is largely similar for all three sensors, with the pMOS and nMOS designs consisting of six lithography steps whereas the dual channel sensor requires eight lithography steps, two additional lithography needed for the formation of the P/N well and source/drain regions.

Table 6 also shows the sensitivity comparison of our sensors with that of several reported work in literature. These comparisons show that our bridge sensors achieve comparable and even superior performance relative to existing design, including cantilever-based structures, which are typically more sensitive than bridge configurations. The higher sensitivity reported in [37] is attributed to its multi-beam array structure. In contrast, the proposed single-beam bridge sensor achieves comparable performance with lower structural complexity and simpler CMOS integration.

Further work was done to study the effect of bridge thickness on sensor sensitivity. Five different bridge thicknesses (1, 2, 3, 4 and 5) µm were simulated, and the results show that lower thickness leads to higher sensitivity, as shown in Table 7. This is because thinner bridge structures exhibit lower stiffness and undergo greater deflection under the same applied load, resulting in larger output variation. However, extremely thin structures may introduce fabrication complexities, increased fragility during mass loading, and reduced structural robustness during handling and operation. This highlights the need for a tradeoff between sensitivity, structural reliability and fabrication complexity in sensor design.

## 4. Conclusion

This study investigates CMOS-MEMS integrated mass sensors with three different configurations. Among them, the dual-channel sensor demonstrated the highest sensitivity of 12.67 µV/µg, significantly outperforming the pMOS and nMOS sensors with sensitivities of 0.11 µV/µg and 2.33 µV/µg, respectively. In addition to superior performance, the

dual-channel sensor also offers the advantages of being fully CMOS-compatible and does not require any external component. Comparison with previously reported sensors shows that our sensors are comparable, and in some cases, outperforms existing works including cantilever-based sensors, which are typically considered more sensitive but are fragile and less stable than bridge structures. The effect of microbridge thickness on sensor sensitivity was also examined. The fabrication process steps for the sensor were also presented. Future works will focus on sensor fabrication and experimental characterization of the proposed sensors.

**Table 4.** Electrical parameters of the proposed current mirror mass sensors under 100 µg load.

| Parameters | p-channel MOSFET mass sensor | | n-channel MOSFET mass sensor | | Dual channel mass sensor | |
|---|---|---|---|---|---|---|
| | M1 | M2 | M1 | M2 | M1 | M2 |
| Gate to source voltage, $V_{GS}$ (V) | 5.976 | 5.976 | 4.024 | 4.024 | 5.976 | 5.976 |
| Drain current, $I_D$ (µA) | 337.007 | 337.008 | 337.007 | 336.994 | 337.007 | 336.997 |
| Drain to source voltage, $V_{DS}$ (V) | 4.02395 | 4.02396 | 4.02395 | 4.02418 | 5.97605 | 5.97478 |
| Output voltage, $V_{out}$ (µV) | $(V_{DS1} - V_{DS2}) = 10$ | | $(V_{DS1} - V_{DS2}) = 230$ | | $(V_{DS1} - V_{DS2}) = 1270$ | |

**Table 5.** Variation of electrical parameters and sensitivity of the proposed sensors with temperature under 100 µg.

| Sensor type | Temperature (K) | Channel resistance (kΩ) | Mobility ($cm^2/Vs$) | Drain voltage (V1) | Drain voltage (V2) | Sensitivity (µV/ µg) |
|---|---|---|---|---|---|---|
| p-channel MOSFET mass sensor | 300 K | 197.9433 | 249.9687 | 4.02376 | 4.02377 | 0.1 |
| | 325 K | 198.0341 | 249.8540 | 4.02308 | 4.02309 | 0.1 |
| | 350 K | 198.1223 | 249.7427 | 4.02242 | 4.02243 | 0.1 |
| n-channel MOSFET mass sensor | 300 K | 592.9951 | 750.5868 | 4.02297 | 4.02320 | 2.3 |
| | 325 K | 591.21 | 752.8428 | 4.01939 | 4.01962 | 2.3 |
| | 350 K | 589.4231 | 755.1010 | 4.01582 | 4.01605 | 2.3 |
| Dual channel mass sensor | 300 K | 197.9452 | 249.9663 | 5.97711 | 5.97585 | 12.6 |
| | 325 K | 198.0392 | 249.8476 | 5.98093 | 5.97967 | 12.6 |
| | 350 K | 198.1247 | 249.7397 | 5.9847 | 5.98344 | 12.6 |

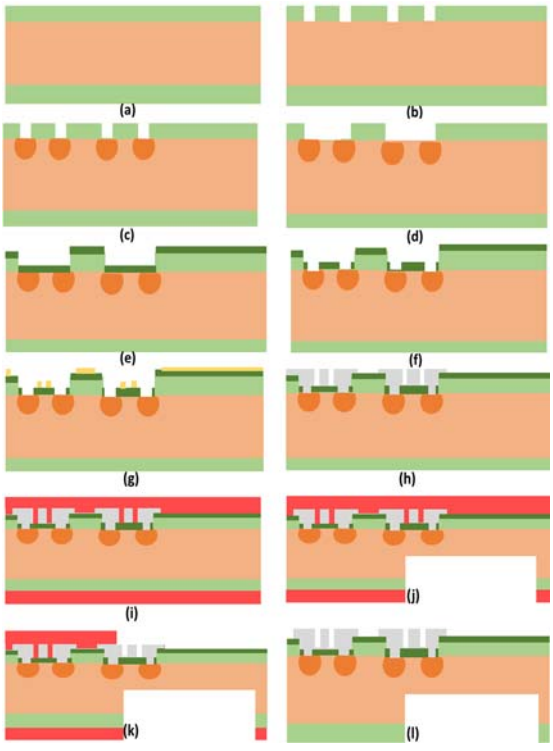


**Fig. 13.** Fabrication process flow of pMOS mass sensor.

**Table 6.** Comparison of proposed sensors with other works reported in literature.

| Type of work | Sensitivity (µV/µg) | Ref. |
|---|---|---|
| Simulation and experimental | 18.87 | [39] |
| Simulation and experimental | 0.515 | [40] |
| Experimental | 0.024 | [41] |
| Experimental | 0.219 | [42] |
| Experimental | 5.299 | [43] |
| Simulation | 0.11 (pMOS)<br>2.33 (nMOS)<br>12.67 (dual) | This work |

**Table 7.** Effect of bridge thickness on sensor sensitivity.

| Thickness of bridge (µm) | Sensor sensitivity (µV/µg) | | |
|---|---|---|---|
| | pMOS | nMOS | Dual channel |
| 1 | 1.44 | 32.13 | 173.99 |
| 2 | 0.55 | 12.04 | 65.44 |
| 3 | 0.24 | 6 | 32.41 |
| 4 | 0.14 | 3.55 | 19.21 |
| 5 | 0.11 | 2.33 | 12.67 |

## Acknowledgements

The authors acknowledge the National Institute of Technology Meghalaya for providing institute overhead funds from the DRDO-sponsored project (Ref: DFTM/07/3603/DIA-CoE,MZU/MEMS/P-03) for the payment of publication fees. The authors also acknowledge the use of a high-end desktop computer purchased under the ISRO-sponsored project (Ref: ISRO/RES/3/807/18-19) for carrying out the simulations reported in this work.

## References

[1]. A. C. R. Grayson, R. S. Shawgo, A. M. Johnson, N. T. Flynn, et al., A BioMEMS review: MEMS technology for physiologically integrated devices, *Proceedings of the IEEE*, Vol. 92, Issue 1, 2004, pp. 6-21.

[2]. F. Khoshnoud, C. W. de Silva, Recent advances in MEMS sensor technology–biomedical applications, *IEEE Instrumentation & Measurement Magazine*, Vol. 15, Issue 1, 2012, pp. 8-14.

[3]. Y. Pandey, S. P. Singh, Recent advances in bio-MEMS and future possibilities: An overview, *Journal of The Institution of Engineers (India): Series B*, Vol. 104, Issue 6, 2023, pp. 1377-1388.

[4]. G. S. Lakshmi, S. R. Karumuri, P. A. Sridhar, J. Akhtar, et al., Design and performance analysis of a microbridge and microcantilever-based MEMS pressure sensor for glucose monitoring, *IEEE Sensors Journal*, Vol. 23, Issue 5, 2023, pp. 4589-4596.

[5]. C. Chircov, A. M. Grumezescu, Microelectro-mechanical systems (MEMS) for biomedical applications, *Micromachines*, Vol. 13, Issue 2, 2022, 164.

[6]. P. Amiri, Z. Kordrostami, M. N. S. Ashkezari, Design of a MEMS bionic vector hydrophone with piezo-gated MOSFET readout, *Microelectronics Journal*, Vol. 98, 2020, 104748.

[7]. C. L. Dai, P. H. Kao, M. C. Liu, C. C. Wu, et al., Micro FET pressure sensor manufactured using CMOS-MEMS technique, *Microelectronics Journal*, Vol. 39, Issue 5, 2008, pp. 744-749.

[8]. H. Baltes, O. Brand, A. Hierlemann, D. Lange, et al., CMOS MEMS-present and future, in *Proceedings of the 15th IEEE International Conference on Micro Electro Mechanical Systems (MEMS)*, 2002, pp. 459-466.

[9]. H. H. Tsai, C. F. Lin, T. P. Sun, C. P. Jiang, et al., Multiple type biosensors fabricated using the CMOS BioMEMS platform, *Sensors and Actuators B: Chemical*, Vol. 144, Issue 2, 2010, pp. 407-412.

[10]. Y. K. Yen, C. Y. Chiu, A CMOS MEMS-based membrane-bridge nanomechanical sensor for small molecule detection, *Scientific Reports*, Vol. 10, Issue 1, 2020, 2931.

[11]. A. A. Zope, J. H. Chang, M. C. Lin, C. H. Chen, et al., A CMOS-MEMS thermal-piezoresistive oscillator for mass sensing applications, *IEEE Transactions on Electron Devices*, Vol. 67, Issue 3, 2020, pp. 1183-1191.

[12]. Y. C. Lee, M. L. Hsieh, Y. C. Chou, C. H. Cheng, et al., CMOS-MEMS technologies for the applications of environment sensors and environment sensing hubs, *Journal of Micromechanics and Microengineering*, Vol. 31, Issue 7, 2021, 074004.

[13]. G. Vidal-Álvarez, E. Marigó, J. J. Sánchez, A. Uranga, et al., Fabrication and measurement of a suspended nanochannel microbridge resonator monolithically integrated with CMOS readout circuitry, *Micromachines*, Vol. 7, Issue 3, 2016, 40.

[14]. Z. J. Davis, W. Svendsen, A. Boisen, Design, fabrication and testing of a novel MEMS resonator for mass sensing applications, *Microelectronic Engineering*, Vol. 84, Issue 5-8, 2007, pp. 1601-1605.

[15]. Z. Hu, J. Hedley, C. McNeil, Design, fabrication and characterization of a piezoelectric MEMS diaphragm resonator mass sensor, *Journal of Micromechanics and Microengineering*, Vol. 23, Issue 12, 2013, 125019.

[16]. P. Joshi, S. Kumar, M. M. Hossain, M. T. Lemaire, et al., Distributed MEMS mass-sensor based on piezoelectric resonant micro-cantilevers, *Journal of Microelectromechanical Systems*, Vol. 28, Issue 3, 2019, pp. 382-389.

[17]. M. U. Nathani, H. Nazemi, P. Hashemi, Capacitive based micromachined resonators for low level mass detection, *Micromachines*, Vol. 12, Issue 1, 2020, 13.

[18]. K. Meinel, C. Stoeckel, C. Weiss, S. Sorge, et al., Piezoelectric scanning micromirror with built-in sensors based on thin film aluminum nitride, *IEEE Sensors Journal*, Vol. 21, Issue 8, 2020, pp. 9682-9689.

[19]. R. M. Pinto, P. Brito, T. I. B. Marques, J. P. Conde, et al., Thin-film silicon MEMS for dynamic mass sensing in vacuum and air: Phase noise, Allan deviation, mass sensitivity and limits of detection, *Journal of Microelectromechanical Systems*, Vol. 28, Issue 3, 2019, pp. 390-400.

[20]. S. Beeby, MEMS Mechanical Sensors, *Artech House*, Norwood, 2004.

[21]. G. Shekhawat, S. H. Tark, V. P. Dravid, MOSFET-embedded microcantilevers for measuring deflection in biomolecular sensors, *Science*, Vol. 311, Issue 5767, 2006, pp. 1592-1595.

[22]. E. L. Gardner, A. De Luca, F. Udrea, Thin-film MOSFET-based pressure sensor, *IEEE Sensors Letters*, Vol. 3, Issue 7, 2019, pp. 1-4.

[23]. P. Singh, J. Miao, G. Li, C. S. Premachandran, et al., Microcantilever sensors with embedded piezoresistive transistor read-out: Design and characterization, *Sensors and Actuators A: Physical*, Vol. 171, Issue 2, 2011, pp. 178-185.

[24]. M. Tetseo, K. Gogoi, S. Kumar, A conceptual study on novel current mirror integrated cantilever (CMIC) mass sensor for micro-gram (μg) range sensing applications, *Microsystem Technologies*, Vol. 30, Issue 3, 2024, pp. 263-275.

[25]. A. T. Bradley, R. C. Jaeger, J. C. Suhling, K. J. O'Connor, Piezoresistive characteristics of short-channel MOSFETs on (100) silicon, *IEEE Transactions on Electron Devices*, Vol. 48, Issue 9, 2001, pp. 2009-2015.

[26]. P. K. Rathore, B. S. Panwar, J. Miao, C. C. Keng, A novel CMOS-MEMS integrated pressure sensing structure based on current mirror sensing technique, *Microelectronics International*, Vol. 32, Issue 2, 2015, pp. 81-95.

[27]. S. Kumar, P. K. Rathore, G. D. Ropmay, P. B. Gogoi, et al., Development of a current mirror-integrated pressure sensor using CMOS-MEMS cofabrication techniques, *Microelectronics International*, Vol. 35, Issue 4, 2018, pp. 203-210.

[28]. S. Kumar, G. D. Ropmay, B. S. Panwar, Fabrication and testing of PMOS current mirror-integrated MEMS

pressure transducer, *Sensor Review*, Vol. 40, Issue 2, 2020, pp. 141-151.
[29]. S. Kumar, G. D. Ropmay, B. S. Panwar, Design and simulation of a novel dual current mirror based CMOS-MEMS integrated pressure sensor, *IET Science, Measurement & Technology*, Vol. 15, Issue 3, 2021, pp. 268-278.
[30]. Y. J. Huang, C. W. Huang, F. C. Ku, M. C. Lin, et al., A CMOS cantilever-based label-free DNA SoC with improved sensitivity for hepatitis B virus detection, *IEEE Transactions on Biomedical Circuits and Systems*, Vol. 7, Issue 6, 2013, pp. 820-831.
[31]. K. W. Li, Y. K. Yen, Gentamicin drug monitoring for peritonitis patients by using a CMOS-BioMEMS-based microcantilever sensor, *Biosensors and Bioelectronics*, Vol. 130, 2019, pp. 420-426.
[32]. Y. K. Yen, C. Y. Lai, Portable real-time detection of Pb (II) using a CMOS MEMS-based nanomechanical sensing array modified with PEDOT: PSS, *Nanomaterials*, Vol. 10, Issue 12, 2020, 2454.
[33]. S. Shin, N. E. Lee, J. S. Park, S. S. Lee, et al., Piezoelectrically driven microtransducer mass sensors, *Integrated Ferroelectrics*, Vol. 80, Issue 1, 2006, pp. 355-362.
[34]. A. S. Sedra, K. C. Smith, Microelectronic Circuits (5th Ed.), *Oxford University Press*, New York, 2004.
[35]. M. Bao, Analysis and Design Principles of MEMS Devices, *Elsevier*, Amsterdam, 2005.
[36]. G. Cadet, M. Paredes, Convergence analysis and mesh optimization of finite element analysis related to helical springs, *Mechanics & Industry*, Vol. 25, 2024, 22.
[37]. T. Nguyen, T. Dinh, A. R. M. Foisal, M. T. Phan, et al., Advances in ultrasensitive piezoresistive sensors: From conventional to flexible and stretchable applications, *Materials Horizons*, Vol. 8, Issue 8, 2021, pp. 2123-2150.
[38]. H. Nyquist, Thermal agitation of electric charge in conductors, *Physical Review*, Vol. 32, Issue 1, 1928, pp. 110-113.
[39]. S. Liu, D. F. Wang, X. B. Chen, Highly sensitive mass sensing scheme via energy relocalization with a coupled three-beam array, *IEEE Sensors Journal*, Vol. 22, Issue 19, 2022, pp. 18400-18408.
[40]. J. Wei, S. Magnani, A. Rastegar, Suspended submicron silicon-beam for high sensitivity piezoresistive force sensing cantilevers, *Sensors and Actuators A: Physical*, Vol. 186, 2012, pp. 80-85.
[41]. M. Ahmed, M. M. Chitteboyina, S. Bhattacharya, MEMS force sensor in a flexible substrate using nichrome piezoresistors, *IEEE Sensors Journal*, Vol. 13, Issue 10, 2013, pp. 4081-4089.
[42]. D. Grech, A. Tarazona, P. G. R. Smith, S. P. Beeby, et al., A quasi-concertina force-displacement MEMS probe for measuring biomechanical properties, *Sensors and Actuators A: Physical*, Vol. 275, 2018, pp. 67-74.
[43]. T. C. Duc, J. Creemer, P. M. Sarro, Piezoresistive cantilever beam for force sensing in two dimensions, *IEEE Sensors Journal*, Vol. 7, Issue 1, 2007, pp. 96-104.